BNL-20076
Conf-751106--1

A Nonsteady Heat Conduction Code with Radiation Boundary Conditions*

J. A. Fillo,** R. Benenati,*** J. Powell**

Abstract

A heat-transfer model for studying the temperature build-up in graphite blankets for fusion reactors is presented. In essence, the computer code developed is for two-dimensional, nonsteady heat conduction in heterogeneous, anisotropic solids with nonuniform internal heating. Thermal radiation as well as bremsstrahlung radiation boundary conditions are included. Numerical calculations are performed for two design options by varying the wall loading, bremsstrahlung, surface layer thickness and thermal conductivity, blanket dimensions, time step and grid size.

Introduction

One area of interest in the fusion reactor program for magnetically confined plasmas is the development of minimum radioactivity, or simply, minimum activation blankets. Blankets make up the region outside the vacuum wall surrounding the plasma. The purpose for the blanket is to convert the kinetic energy of the high energy neutrons which are due to the fusion reaction to heat as well as breed tritium from the lithium contained in the blanket.

*This research was carried out under the auspices of U.S. Energy Research and Development Administration.

**Department of Applied Science, Brookhaven National Laboratory, Upton, New York 11973.

***Consultant; Professor of Chemical Engineering, Polytechnic Institute of New York, Brooklyn, New York 10030.

While a number of minimum activation blanket concepts have been proposed, operating life is limited by radiation damage to several years at 1 MW/m^2 first wall loading. At Brookhaven National Laboratory, on the other hand, minimum activation blanket designs [1]* are being investigated which reduce the radiation damage to the blanket coolant-system by an order of magnitude or more compared with previous designs, as well as permitting blanket operating lives up to 30 years--the life of a reactor.

The basis for reducing the radiation damage is to impose a graphite screen between the plasma and the blanket coolant structure. Figure 1 depicts one possible design configuration. To reduce the impurity concentration to the plasma, the graphite surface temperature (T_s) is limited to 2300°K. The graphite surface in the various designs is shaped to keep T_s <2300°K by radiant heat transfer alone. This is accomplished by introducing a low-conductivity surface-layer of graphite, (e.g., pyrographite or a graphite fibrous mat). This necessitated the development of a heat-conduction code with thermal radiation as well as bremsstrahlung radiation boundary conditions.

Physical Description of Proposed System

Heat enters the surface of the graphite blanket via: (a) bremsstrahlung radiation, (b) neutron-gamma reactions within the graphite, and (c) neutron deposition energy. In turn, most of the energy deposited on and in the graphite by bremsstrahlung, neutrons, and gamma rays is radiated away from the surface to a sink, (e.g., a portion of the blanket surface conventionally constructed of low temperature [600°] materials cooled by helium). The balance, deposited inside the blanket, is either (a) stored during the plasma burn and then removed by direct cooling when

*Numbers in brackets designate References at end of report.

the reactor shuts down (Figure 1), or (b) radiated to a secondary blanket with coolant tubes (Figure 2). Both cases are considered in this study.

Governing Equations

For our system we consider a small but finite rectangular element of unit-depth fixed in space. Applying the first law of thermodynamics to the system and relating the rate of heat-flow through an area of the element by Fourier's law, the two-dimensional finite difference equations for nonsteady heat conduction and with nonuniform internal heat-generation may be written as

$$\sum_{i=1}^{4} K_{ij}(T_i - T_j) + Q_j \Delta V_j = \rho_j c_j \Delta V_j \frac{dT_j}{dt} \qquad (1)$$

where $K_{ij} = \dfrac{1}{\dfrac{\ell_{ij}}{k_{ij}A_{ij}} + \dfrac{\ell_{ji}}{k_{ji}A_{ji}}}$. In the present notation i represents the nodes surrounding the node of interest, j; (for reference see Figure 3a). Heterogeneous, anisotropic solids are admitted in the formulation; (i.e., at each node thermal properties may be temperature dependent and, in addition, the thermal conductivity may be orientation dependent). The interface condition for nodes surrounding the node of interest is specified by maintaining continuous thermal flux at the boundary.

For unsteady heat conduction the time derivative, $\dfrac{dT_j}{dt}$ is made discrete by introducing the forward difference expression

$$\frac{dT_j}{dt} = \frac{T_j\,(\text{NEW}) - T_j\,(\text{OLD})}{\Delta t} = \frac{T_j^{n+1} - T_j^{n}}{\Delta t} \qquad (2)$$

In addition, the left hand side of Eq. (1) is assumed to be evaluated at the "old" time (i.e., at time n). This results in

the standard explicit method; the temperature at time n+1 is an explicit function of the known temperatures and internal heat generation at time n. Eq. (1) can now be written as

$$T_j^{n+1} = T_j^n + \frac{\Delta t}{\rho_j c_j \Delta V_j}\left[\sum_{i=1}^{4} K_{ij}^n \,(T_i^n - T_j^n) + Q_j^n\right] \qquad (3)$$

Eq. (3) must be modified to account for boundary conditions.

While the computer code has been developed for such geometries as depicted in Figures 1 and 2, in Appendix A we only consider the finite difference formulation of the boundary conditions for the physical case in Figure 1.

The computer program is written entirely in FORTRAN IV and consists of four principle routines to handle data input, radiant view factor determination, step-by-step solutions of the heat balance of all nodal points, and print-out of final results. Data input has been simplified to the maximum extent possible while maintaining a large degree of flexibility in the specifics of the structure being analyzed. Eighteen node-types have been identified and constitute the basic building blocks used to describe the structure. At the present time, the system consists of a grid containing 500 nodes and up to 61 radiant streams to a given surface node. These figures may be increased.

Graphite Blanket Test Case

For the first test case we consider the blanket design shown in Figure 1. Ordinary graphite is assumed throughout but a variable is the surface layer, typically 0.5 cm to 1.0 cm, which may be pyrographite or a graphite fibrous mat. For tritium breeding, a layer of lithium aluminate (Li^6AlO_2) ceramic is inserted at the base of the cavity. During cooling the tritium diffuses to the coolant stream (e.g., helium) and is carried away for processing.

An important parameter in blanket fusion studies is the wall loading (WL). It is defined as the total thermal fusion power divided by the surface area of the torus, the reactor area which faces the plasma. That is, we assume a Tokamak device. Being able to operate at higher wall loadings than $1 MW/m^2$ is significant from an economic standpoint, namely, reactor costs. For example, for a given plasma configuration and set of operating conditions, the total thermal fusion power is fixed. Reducing the torus area in proper proportion with increased wall loading could leave the same total fusion power as with a larger reactor. In general, what limits the wall loading are the temperatures at which the blanket operates. Various wall loadings above 1 MW/m^2 are considered in the study.

Bremsstrahlung radiation plays an important role in limiting the operating temperatures of the blanket. Brookhaven has studies under way examining means to reduce the bremsstrahlung. Reduced bremsstrahlung combined with high wall loading is most desirable. The parameter, Po, a measure of the bremsstrahlung radiation, is varied in our study. Table I is a listing of the material and thermal properties used in the investigations.

Computed Results and Discussion

The purpose of this section is to discuss results which demonstrate the feasibility of applying the present heat transfer model to the design of graphite blankets.

A. Direct Cooling During Shutdown

For this design case the operating time of the blanket is governed by the temperature build-up in the blanket and subsequent limiting temperatures. That is, since the blanket can absorb energy for several hundred seconds before limiting temperatures are reached, several plasma burns or possible one continuous burn can

be accommodated during the blanket heat-up phase without having cooling until limiting temperatures are reached. Optimum cycles favor relatively long plasma burns and relatively short cooling and pumpdown times. Hence the longer the build-up time in the blanket before limiting temperatures are reached, so much the better for the graphite blanket concept.

Table II provides a summary of the test runs made. The effects of wall loading, bremsstrahlung radiation, Po, surface layer thermal conductivity, cavity height, time-step, and grid-size parameters were all examined.

Figure 4 is a plot of the neutron + gamma heat-deposition rates per unit volume for WL = 1.0 MW/m^2. These results are for the case when D_1 = 50 cm. The heat deposition rates for the higher wall loadings, 2.0 and 3.0 MW/m^2, are obtained by multiplying the results of Figure 4 by 2.0 and 3.0, respectively.

The effect of grid size was investigated in runs Nos. 1 and 2 by reducing the vertical grid spacing from 2 cm to 1 cm in the cavity region. Temperature profiles varied by no more than 0.05% at equivalent grid locations. The effect of time-step was investigated in run No. 3 by doubling the time-step from 1 to 2 sec with virtually no change in temperature profiles at equivalent times.

It is of interest that no stability problems were encountered even though the explicit method was used. As noted in Appendix A since a low conductivity surface layer is introduced, the dominant factor controlling stability are the internal nodes and not the boundary effects. The internal heating never gets too large to cause problems. For a system of 300 nodes and a time-step of 1 sec, computer runs for burn times of 1000 sec were executed in 22 sec including program compilation.

A series of surface layer temperature profiles are presented in Figure 5 for the conditions of run No. 1 and runs Nos. 4 to 8. It is clear that the blanket performance is improved by introducing a pyrographite surface layer; (i.e., operating times are extended over a pure graphite blanket). In particular for a wall loading of 2 MW/m^2, operating time increases by ≈100 sec. There does not appear to be any temperature problems for the pure graphite case at wall loadings of 1 MW/m^2. Figure 6 emphasizes the importance or need to reduce bremsstrahlung radiation in order to successfully operate at higher wall loadings (e.g., 3 MW/m^2) for substantial operating periods. The operating time is extended by over a 100 sec with a 50% reduction in Po.

Temperature profiles at 1.5 cm from the surface are presented in Figure 7 for the conditions of runs Nos. 6 and 7. These temperatures are less than the surface temperatures at the lower end of the time-scale but become greater than the surface layer as time increases. Within the time governed by the limiting surface temperature, the internal temperatures never build up to values which exceed internal breakdown. Temperatures deeper in the blanket are less, of course. Figure 8 is a typical temperature plot for the blanket. One sees a marked reduction in temperatures in the lower portions of the blanket in comparison with the surface region and the effect of thermal radiation exchange between surfaces.

Runs Nos. 10 to 12 depict the effect of increasing the cavity region. Figure 9 is a plot of surface-layer temperatures for varying wall loading and is to be compared with Figures 5 and 6 to ascertain the effect of changing the cavity dimensions. No noticeable effect on the surface layer temperature is observed (i.e., a thinner graphite screening region does not extend the operating

plasma burn time). The blanket at equivalent vertical locations, if anything, tends to run hotter than the case when D_1 = 50 cm.

A series of surface-layer temperature profiles are presented in Figure 10 for the low-conductivity layer runs (Nos. 14 to 16). Physically this might be the case for a fibrous graphite mat. These results do not include the effect of reduced density in the surface layer as a consequence of the fibrous mat. The surface layer is assumed to be 0.5 cm thick. While the temperatures appear to be most encouraging (especially the 3.0 MW/m^2 loading), Po = 12.75 W/cm^2 (compare with Figure 6) where the burn time is extended to 500 sec, the results are deceptive. The internal temperatures in the blanket become too hot, in some instances 2800°K. On the other hand, the thermal conductivity values for the mat were assumed and may be too low. The density effect must also be checked. An additional material combination may be a fibrous mat, pyrographite, and ordinary graphite blanket. No calculations have been made for this case though.

Figure 11 (runs Nos. 6 to 8) is a study of the effect of reduced initial blanket temperature with respect to burn time. While the burn time is extended to 800 sec for a wall loading of 2 MW/m^2 before limiting blanket temperatures set in, the 3 MW/m^2 loading is less dramatic. A gain of slightly more than 100 sec is achieved. Clearly, as low an initial blanket temperature as possible is desirable.

B. Secondary Blanket With Coolant Tubes

This design case differs from Case A in that coolant tubes are placed at the base of the cavity. Continuous cooling takes place. The energy deposited in the blanket near the surface is thermally radiated down the cavity channels between the blocks to the secondary blanket where it is absorbed by coolant tubes.

Of interest is whether or not a steady-state temperature distribution is achieved in the blanket structure during a plasma burn. It was found in our initial test cases that steady-state was not achieved before the limiting surface temperatures were exceeded.

Table III provides a summary of the test runs made. The effect of wall loading and bremsstrahlung radiation were examined. The secondary coolant tubes were assumed to be maintained at the constant temperature (673^{o}K) during the plasma burn. These were placed along the base of the cavity and along the cavity walls for 15 cm (see Figure 2). As a first approximation in the analysis, the surface nodes where the coolant tubes were placed were assumed to be at the constant tube temperature.

A series of surface layer temperature profiles are presented in Figure 12. Of interest is that for 2 and 3 MW/m^2 wall loadings, approximately the same time is reached before the limiting surface temperatures sets in as in Case A. The internal blanket temperatures at equivalent locations are lower in Case B. Obviously, additional test runs with parameter variations are to be made to explore this design further.

In summary, the heat transfer model and computer code which we have developed provide a useful tool for establishing limiting blanket temperatures and design information. The code could be used for other heat transfer applications with thermal radiation boundary conditions so long as the physical structure can be described by some combination of the following node types (all surfaces not explicitly mentioned are conduction faces):

Type	Description
1	an interior node;
2	a surface node with radiation at the upper surface;
3	a surface node with radiation at the right hand surface;

Type (cont'd)	Description
4	a surface node with radiation at the lower surface;
5	a surface node with radiation at the left hand surface;
6	a corner node with radiation at the upper and right hand surfaces;
7	a corner node with radiation at the lower and right hand surfaces;
8	a corner node with radiation at the lower and left hand surfaces;
9	a corner node with radiation at the upper and left hand surfaces;
10	a corner node with radiation at the upper surface and symmetry at left hand surfaces;
11	a corner node with radiation at the upper surface and symmetry at right hand surface;
12	a corner node with radiation at the lower surface and symmetry at right hand surface;
13	a corner node with radiation at the lower surface and symmetry at left hand surface;
14	an edge node with symmetry at right hand surface;
15	an edge node with symmetry at lower surface;
16	an edge node with symmetry at left hand surface;
17	a corner node with symmetry at the lower and right hand surfaces;
18	a corner node with symmetry at the lower and left hand surfaces.

Details of the use of this code may be found in a report, "CONRAD: Heat Conduction-Radiation Code" of the Brookhaven National Laboratory.

Appendix A

Figure 13 is a representation of the model geometry studied. Symmetry is assumed along the western boundary as well as the eastern, the gap width being assumed negligible. Symmetry is also assumed along the southern boundary.

The western boundary condition, specified by $\frac{\partial T}{\partial x} = 0$, is satisfied by setting $T_1 = T_5$ (note Figure 3a). On the eastern boundary $\frac{\partial T}{\partial x} = 0$ is satisfied by setting $T_1 = T_3$ while on the southern boundary where $\frac{\partial T}{\partial y} = 0$, T_1 is set equal to T_4.

The northern boundary experiences radiative energy exchange with the surroundings. The boundary condition is expressed by

$$-kA\frac{\partial T}{\partial y}\Big)_{y=0} = \sigma F\epsilon\left(T_s^4 - T^{*4}\right)A - PoA \qquad (1a)$$

where F is the view factor between the element of area A and the sink area. In our case F = 1.0 since we assume parallel planes and ϵ, the emissivity of the sink area, is taken to be 0.2. In other words, it is assumed that the sink area is ≈20% of the total area. T_s is the surface or boundary temperature of the blanket, and T* is the sink temperature. The plasma is assumed to be perfectly transparent to thermal radiation. Bremsstrahlung radiation from the plasma to the blanket surface is accounted for via Po. This mode of radiation is assumed isotropic.

We assume a zero capacitance surface node. Figure 3b is a portion of the R-C network used in the present formulation. Performing an energy balance on the surface node, we find

$$q_{\text{surroundings}\longrightarrow s} + q_{1\longrightarrow s} = 0. \qquad (2a)$$

or

$$\varepsilon\sigma F\left(T^{*4}-T_s^4\right)A + PoA + \frac{k_{vA}}{\Delta y/2}\left(T_1-T_s\right) = 0$$

Rearranging

$$T_s = T_1 + \frac{\Delta y}{2k_{vA}}\left[\varepsilon\sigma FA\left(T^{*4}-T_s^4\right) + PoA\right] , \qquad (3a)$$

we note that T_s is a function of T_1 which, of course, is an unknown.

An energy balance on 1 results in

$$\varepsilon\sigma F\left(T^{*4}-T_s^4\right) + PoA + Q_1\Delta V_1 1 + K_{31}\left(T_3-T_1\right)$$
$$+ K_{41}\left(T_4-T_1\right) + K_{51}\left(T_5-T_1\right) = \rho_1 c_1 \Delta V_1 \frac{dT_1}{dt} . \qquad (4a)$$

At this point we assume that $T_s = T_1$, eliminating the additional step of solving for the surface node temperature. Since $T_s > T^*$ and Po is positive, we find that the terms in the brackets of Eq. (3a) can be positive or negative, a function of the wall-loading as well as the time (i.e., there is a cancelling effect taking place and at some instant of time the sum may even be zero). The approximation which we have made can be improved by reducing the vertical spacing of the element in which the surface node and node one appear. This does not produce an unduly small time-step for numerical calculations since the component of the thermal conductivity in the vertical direction will be small ($0.02 W/cm^{\circ}K$ for pyrographite or smaller) for the surface layer. This has the effect of increasing the time-step for the surface layer. Hence the time-step for the numerical calculations is primarily dictated by the internal nodes.

A numerical calculation was performed by changing the vertical spacing from 1 cm to ½ cm for a pyrographite surface layer

and for a wall-loading of 1 MW/m^2. It was found that the surface-layer temperatures changed by 0.5% and the internal temperatures by much less. Consequently, our assumption was deemed adequate for our design purposes.

For the internal cavity, black-body radiant-energy exchange is assumed between surfaces. For example referrring to Figure 13, there is radiant interchange between any surface A_j and all surfaces $A_{j'=1}$ through $A_{J'}$ on the opposite side of the cavity. In addition there is interchange between all surfaces $A_{k=1}$ through A_K as well as $A_{m=1}$ through A_M. The radiant flux from A_j that falls on $A_{j'}$ is

$$q_{j-j'} = F_{jj'} e_j A_j \quad , \tag{5a}$$

where

$$F_{jj'} = \frac{\cos^2\theta}{2R} A_{j'} \quad , \quad e_j = \sigma T_j^4 \quad .$$

The view factors (and subsequent view factors) have been developed for the case of two elemental surfaces which see each other. [2] In addition, from Figure 13 we see that

$$\cos\theta = \frac{D_2}{R} \quad \text{and} \quad R = \left[D_2^2 + y_{jj'}^2\right]^{\frac{1}{2}} \quad .$$

The net interchange between j and j' is

$$q_{j\rightleftarrows j'} = \frac{\sigma}{2} \frac{\cos^2\theta}{R} A_j A_{j'} \left(T_j^4 - T_{j'}^4\right) \quad . \tag{6a}$$

The total interchange between j and all j' elements on the opposite side of the slot is then

$$q_{j\rightleftarrows \Sigma j'} = \frac{\sigma}{2} D_2^2 A_j \sum_{j'=1}^{J'} \frac{(T_j^4 - T_{j'}^4) A_{j'}}{(D_2^2 + y_{jj'}^2)^{3/2}} \quad , \tag{7a}$$

which may also be written as

$$q_{j\neq\Sigma j'} = \sum_{j'=1}^{J'} f_{jj'}\left(T_j^4 - T_{j'}^4\right), \tag{8a}$$

where

$$f_{jj'} = \frac{\sigma}{2} \frac{D_2^2}{(D_2^2 + y_{jj'}^2)^{3/2}} A_j A_{j'} \quad . \tag{8b}$$

In a similar development, the interchange between j and all k and m elements may be written as

$$q_{j\neq\Sigma k} = \sum_{k=1}^{K} f_{jk}\left(T_j^4 - T_k^4\right) \tag{9a}$$

$$q_{j\neq\Sigma m} = \sum_{m=1}^{M} f_{jm}\left(T_j^4 - T_m^4\right) \tag{10a}$$

where

$$f_{jk} = \frac{\sigma}{2} \frac{x_{jk} y_{jn}}{(x_{jk}^2 + y_{jk}^2)^{3/2}} A_j A_k \tag{11a}$$

$$f_{jm} = \frac{\sigma}{2} \frac{x_{jm} y_{jm}}{(x_{jm}^2 + y_{jm}^2)^{3/2}} A_j A_m \quad . \tag{11b}$$

The horizontal distances, x_{jk} and x_{jm} and vertical distances, y_{jk} and y_{jm} are measured from j to the node in question, k or m. As in the case of the northern boundary, we assume that the surface temperature is the same as the first node temperature in from the boundary. Referring to Figure 13 and letting node 1 represent any j node (j=1 to J), an energy balance on node 1 yields

$$\sum_{j'=1}^{J'} f_{1j'}\left(T_{j'}^4 - T_1^4\right) + \sum_{k=1}^{K} f_{1k}\left(T_k^4 - T_1^4\right) + \sum_{m=1}^{M} f_{1m}\left(T_m^4 - T_1^4\right)$$

$$+ K_{21}\left(T_2-T_1\right) + K_{41}\left(T_4-T_1\right) + K_{51}\left(T_5-T_1\right) + Q_1\Delta V_1 =$$

$$\rho_1 c_1 \Delta V_1 \frac{dT_1}{dt} \quad . \tag{12a}$$

The forward difference expression, Eq. (2), is introduced to discretize $\frac{dT_1}{dt}$ and all terms on the left hand side of Eq. (12a) are evaluated at time n.

Energy balances for the remaining boundaries result in

m boundary:

$$\sum_{j=1}^{J} f_{1j}\left(T_j^{\,4}-T_1^{\,4}\right) + \sum_{j'=1}^{J'} f_{1j'}\left(T_{j'}^{\,4}-T_1^{\,4}\right) + \sum_{k=1}^{K} f_{1k}\left(T_k^{\,4}-T_1^{\,4}\right)$$

$$+ K_{21}\left(T_2-T_1\right) + K_{31}\left(T_3-T_1\right) + K_{51}\left(T_5-T_1\right) + Q_1\Delta V_1 =$$

$$\rho_1 c_1 \Delta V_1 \frac{dT_1}{dt} \quad . \tag{13a}$$

k boundary:

$$\sum_{j=1}^{J} f_{1j}\left(T_j^{\,4}-T_1^{\,4}\right) + \sum_{j'=1}^{J'} f_{1j'}\left(T_{j'}^{\,4}-T_1^{\,4}\right) + \sum_{m=1}^{M} f_{1m}\left(T_m^{\,4}-T_1^{\,4}\right)$$

$$+ K_{31}\left(T_3-T_1\right) + K_{41}\left(T_4-T_1\right) + K_{51}\left(T_5-T_1\right) + Q_1\Delta V_1 =$$

$$\rho_1 c_1 \Delta V_1 \frac{dT_1}{dt} \tag{14a}$$

where

m boundary:

$$f_{1j} = \frac{\sigma}{2} \frac{x_{1j}y_{1j}}{\left(x_{1j'}^{\,2} + y_{1j'}^{\,2}\right)^{3/2}} A_1 A_{j'} \tag{15a}$$

$$f_{1j'} = \frac{\sigma}{2} \frac{x_{1j'} y_{1j'}}{(x_{1j'}^2 + y_{1j'}^2)^{3/2}} A_1 A_{j'} \qquad (16a)$$

$$f_{1k} = \frac{\sigma}{2} \frac{D_1^2}{(x_{1k}^2 + D_1^2)^{3/2}} A_1 A_k \qquad (17a)$$

k boundary:

$$f_{1j} = \frac{\sigma}{2} \frac{x_{1j} y_{1j}}{(x_{1j}^2 + y_{1j}^2)^{3/2}} A_1 A_j \qquad (18a)$$

$$f_{1j'} = \frac{\sigma}{2} \frac{x_{1j'} y_{1j'}}{(x_{1j'}^2 + y_{1j'}^2)^{3/2}} A_1 A_{j'} \qquad (19a)$$

$$f_{1m} = \frac{\sigma}{2} \frac{D_1^2}{(x_{1m}^2 + D_1^2)^{3/2}} A_1 A_m \qquad (20a)$$

Since the geometry is symmetrical about the center line through the cavity, only one-half of the geometry need be analyzed. Consequently no energy balance for j' elements are written. The computer code has been developed to account for nonsymmetrical geometries as well.

Acknowledgments

Dr. Otto Lazareth performed the calculations for the internal volumetric heating rates. This work was performed under the auspices of U.S. Energy Research and Development Administration.

References

1. Powell, J. and Lazareth, O., "Fusion Blankets with Minimum Activation and Minimum Vulnerability to Radiation Damage," ANS Transactions, Vol. 19, 1974, pp. 17-18.

2. Jacob, M., Heat Transfer, Vol. 2, John Wiley and Sons, Inc., New York, 1957.

Nomenclature

A	=	elemental surface area
A_{ij}, A_{ji}	=	elemental area, normal to the heat flow into or out of an internal element
D_1	=	cavity height
D_2	=	cavity width
F	=	view factor
k_{ij}, k_{ji}	=	thermal conductivity components
K_{ij}	=	term defined in Eq. (3)
ℓ_{ij}, ℓ_{ji}	=	lengths for nodal spacing, defined in Figure 3a.
L_1	=	height of blanket
L_2	=	width of blanket
Po	=	bremsstrahlung radiation/unit area
Q_j	=	internal volumetric heat generation rate, W/cc
t	=	time
Δt	=	time-step
T	=	temperature
T^*	=	sink temperature
ΔV_j	=	elemental volume, node j
WL	=	wall loading
ϵ	=	emissivity
σ	=	Stefan--Boltzmann constant
$\rho_j c_j$	=	heat capacity (density x specified heat) for node j

Table I

MATERIAL AND THERMAL PROPERTIES

	k_h $w/_{cm\,^oK}$	k_v $w/_{cm\,^oK}$	ρ $g/_{cm^3}$	c $cal/_{g\,^oK}$
Graphite	0.5	0.5	1.9	0.5
Pyrographite	1.0	0.02	1.9	0.5
Graphite Fibrous Mat	0.005	0.005	1.9	0.5

Table II

SUMMARY OF TEST RUNS

Run	Surface Layer	Geometry D_1 cm	D_2 cm	L_1 cm	L_2 cm	Grid Size Δx cm	Δy cm	Time Step Δt sec.	WL MW/m^2	Po W/cm^2	ϵ
1	Graphite	50	10	74	10	1	1	1	1	8.5	0.2
2	Graphite	50	10	74	10	1	2*	1	1	8.5	0.2
3	Graphite	50	10	74	10	1	1 2*	2	1	8.5	0.2
4	Graphite	50	10	74	10	1	2*	1	2	17.0	0.2
5	Graphite	50	10	74	10	1	2*	1	3	25.5	0.2
6	Pyrographite	50	10	74	10	1	2*	1	1	8.5	0.2
7	Pyrographite	50	10	74	10	1	2*	1	2	17.0	0.2
8	Pyrographite	50	10	74	10	1	2*	1	3	25.5	0.2
9	Pyrographite	50	10	74	10	1	2*	1	3	12.75	0.2
10	Pyrographite	55	10	74	10	1	2*	1	2	17.0	0.2
11	Pyrographite	55	10	74	10	1	2*	1	3	25.5	0.2
12	Pyrographite	55	10	74	10	1	2*	1	4	17.0	0.2
13	Fibrous Mat	50	10	74	10	1	2*	1	3	25.5	0.2
14	Fibrous Mat	50	10	74	10	1	2*	1	3	12.75	0.2
15	Fibrous Mat	50	10	74	10	1	2*	1	4	17.0	0.2

*The vertical spacing, Δy, was maintained at 1 cm for the first 10 cm and then expanded to 2 cm thereafter.

Table III

SUMMARY OF TEST RUNS

Run	Surface Layer	Geometry D_1 cm	D_2 cm	L_1 cm	L_2 cm	Grid Size Δx cm	Δy cm	Time Step Δt sec.	WL MW/m^2	Po W/cm^2	ϵ
1	Pyrographite	50	10	74	10	1	2*	1	1	8.5	0.2
2	Pyrographite	50	10	74	10	1	2*	1	2	17.0	0.2
3	Pyrographite	50	10	74	10	1	2*	1	3	25.5	0.2

*The vertical spacing, Δy, was maintained at 1 cm for the first 10 cm and then expanded to 2 cm thereafter.

List of Figures

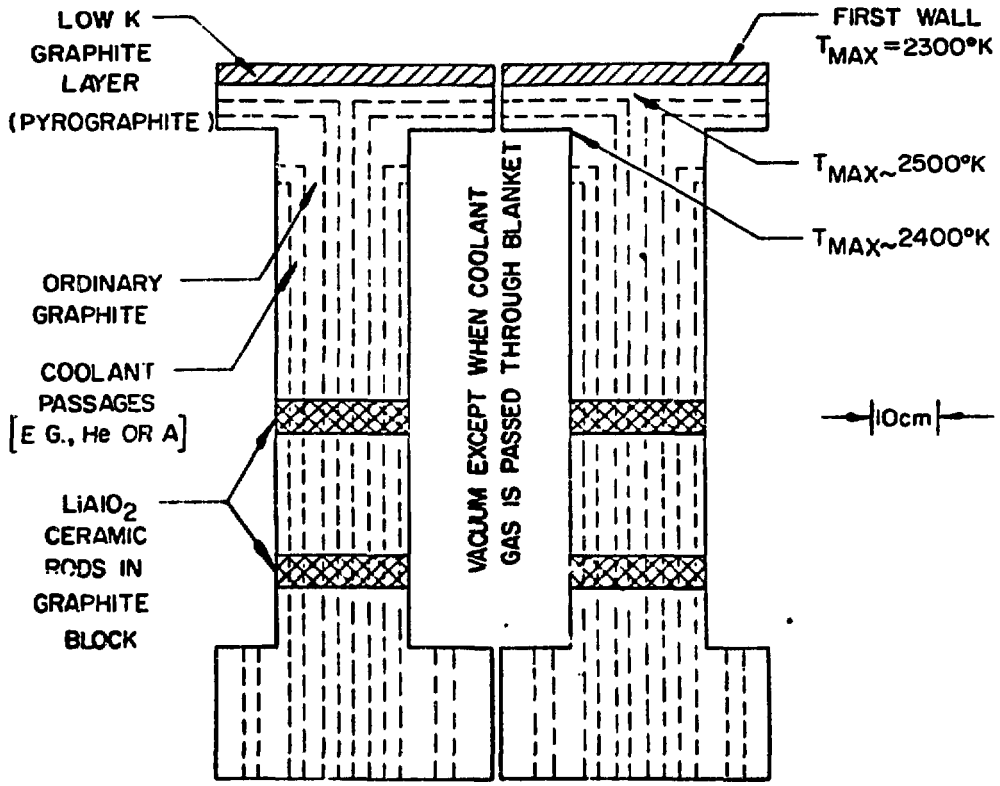

Figure 1

J. Fillo, et. al.

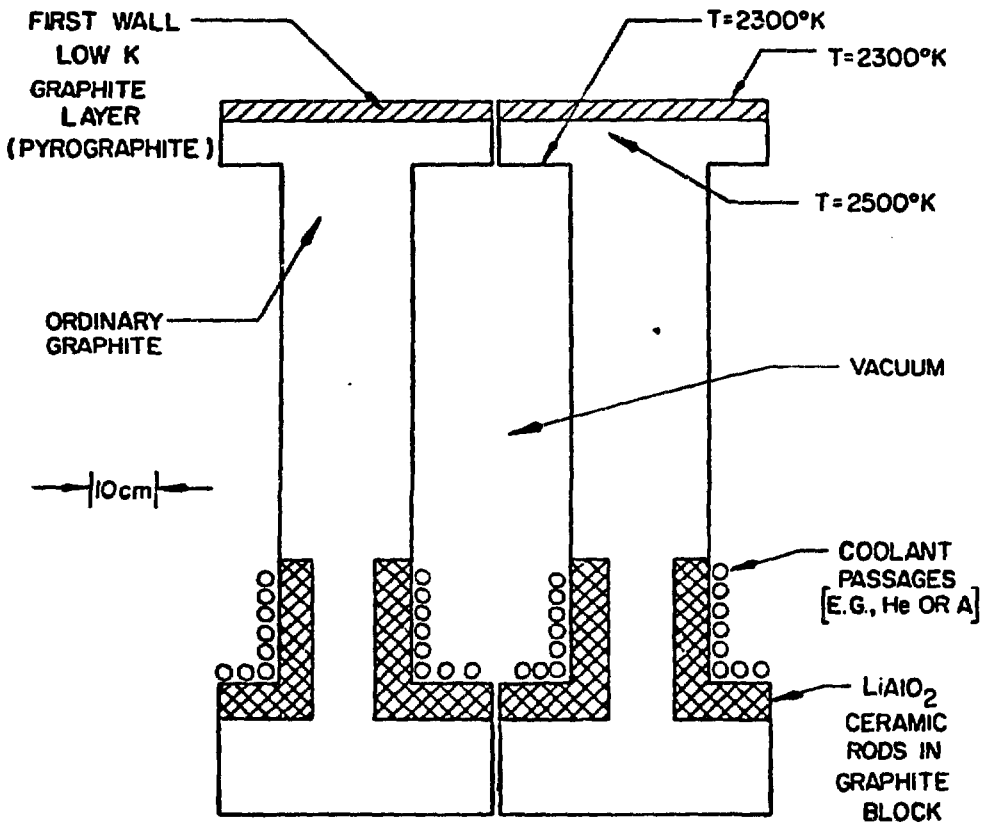

Figure 2

J. Fillo, et. al.

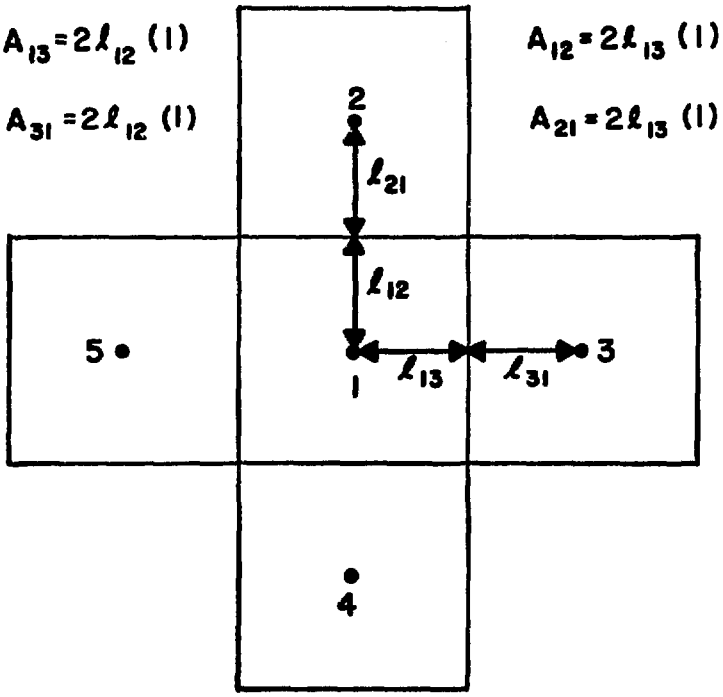
$A_{13}=2\ell_{12}$ (1)
$A_{31}=2\ell_{12}$ (1)
$A_{12}=2\ell_{13}$ (1)
$A_{21}=2\ell_{13}$ (1)
2
ℓ_{21}
ℓ_{12}
5
1
ℓ_{13}
ℓ_{31}
3
4

Figure 3a

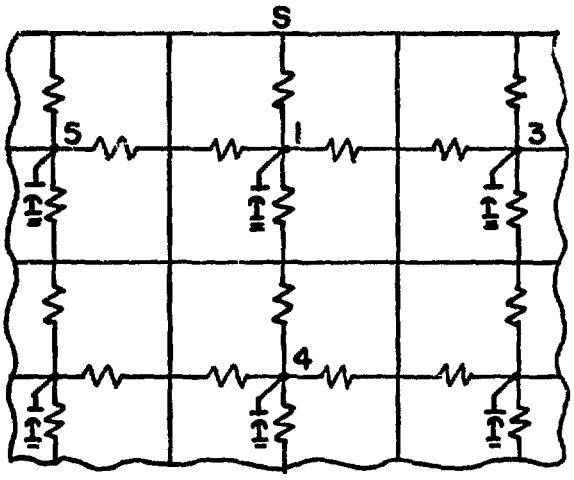

Figure 3b

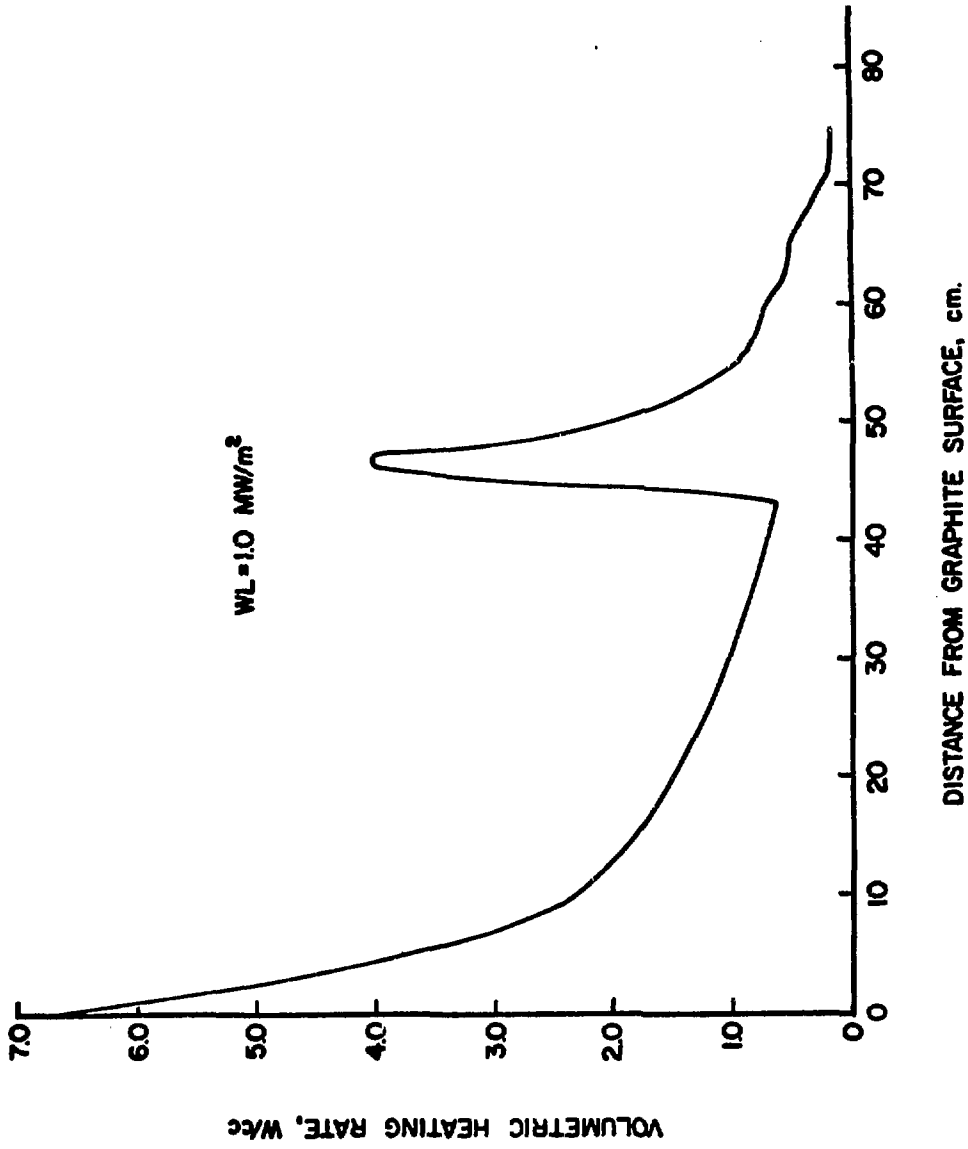

Figure 4

J. Fillo, et. al.

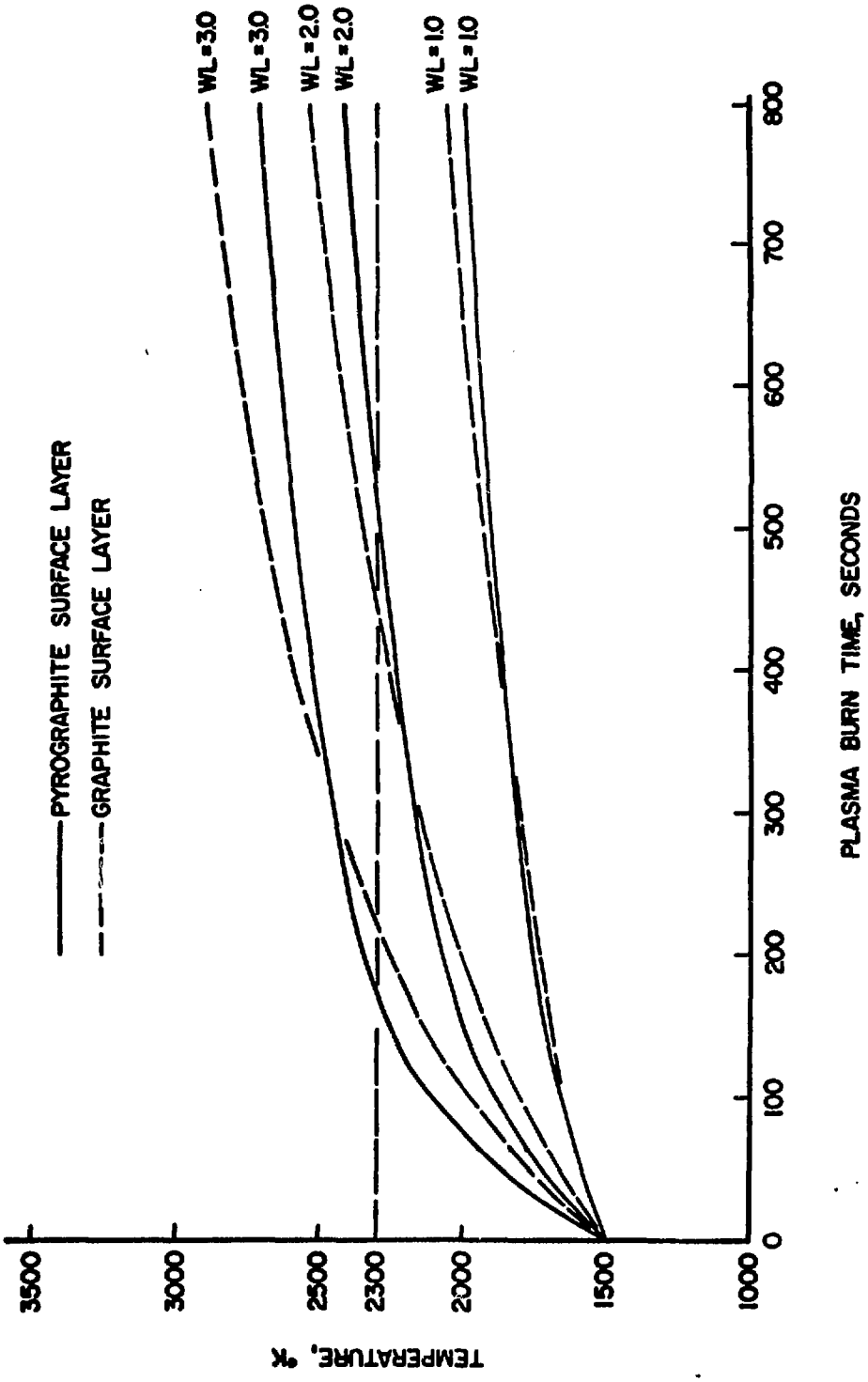

Figure 5

J. Fillo, et. al.

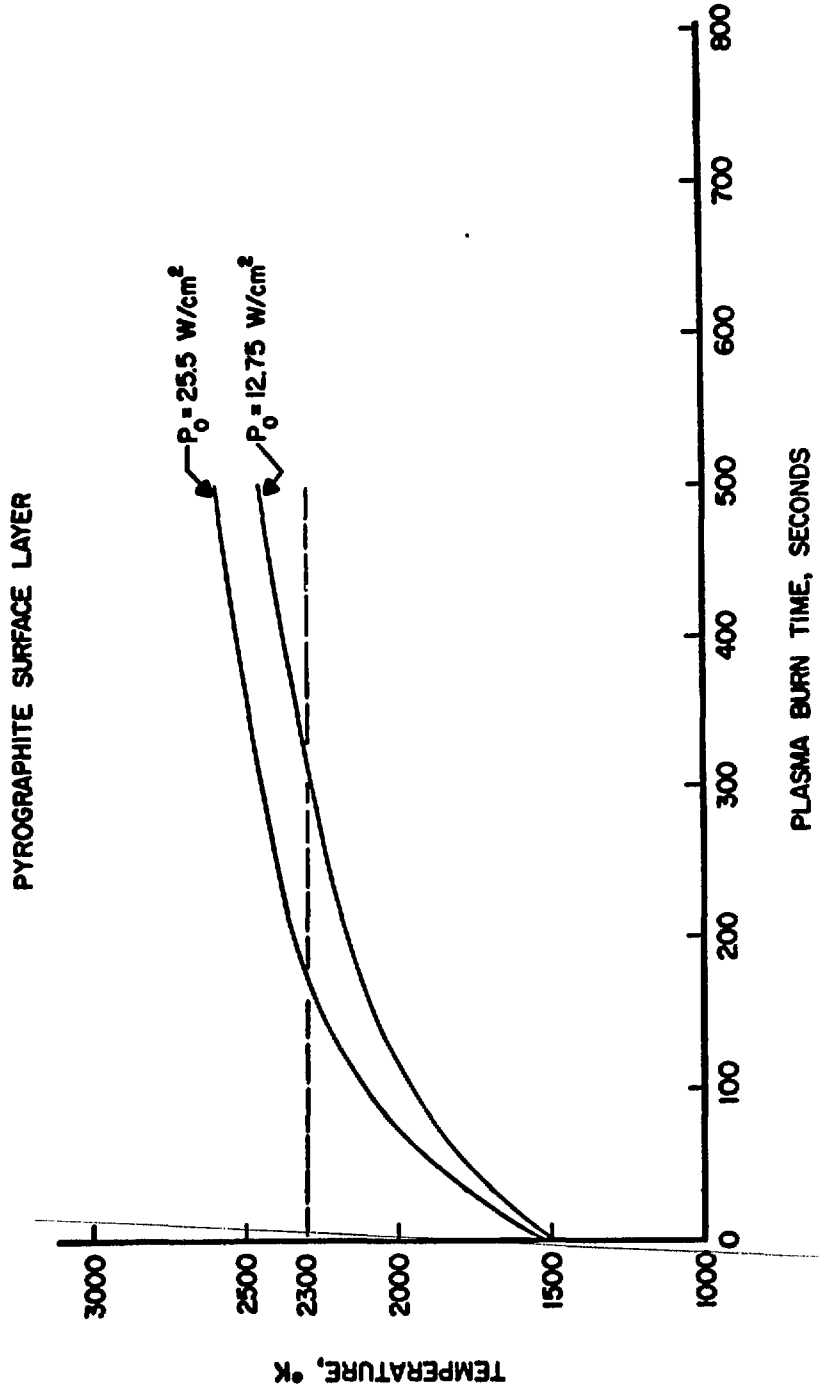

Figure 6

J. Fillo, et. al.

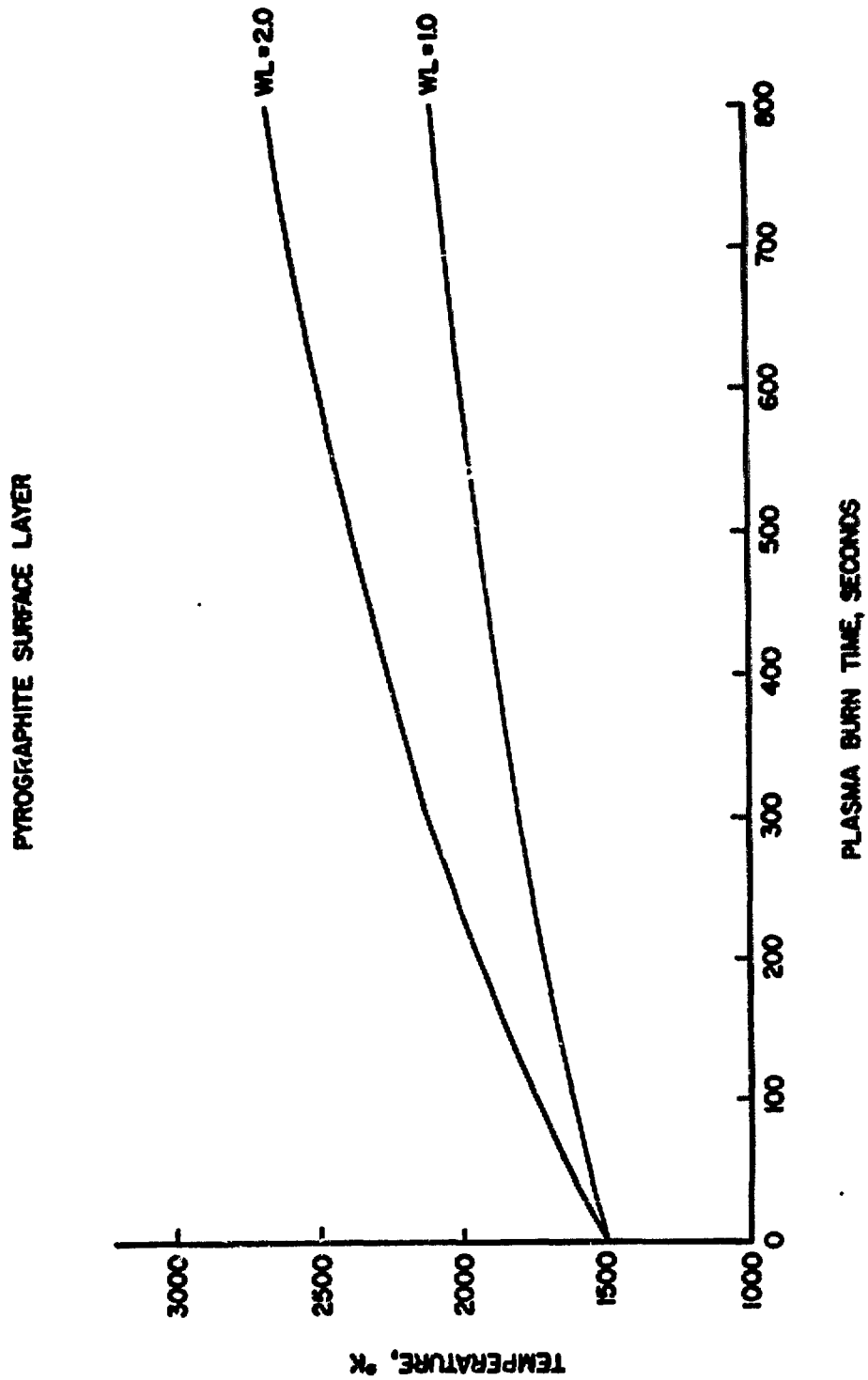

Figure 7

J. Fillo, et. al.

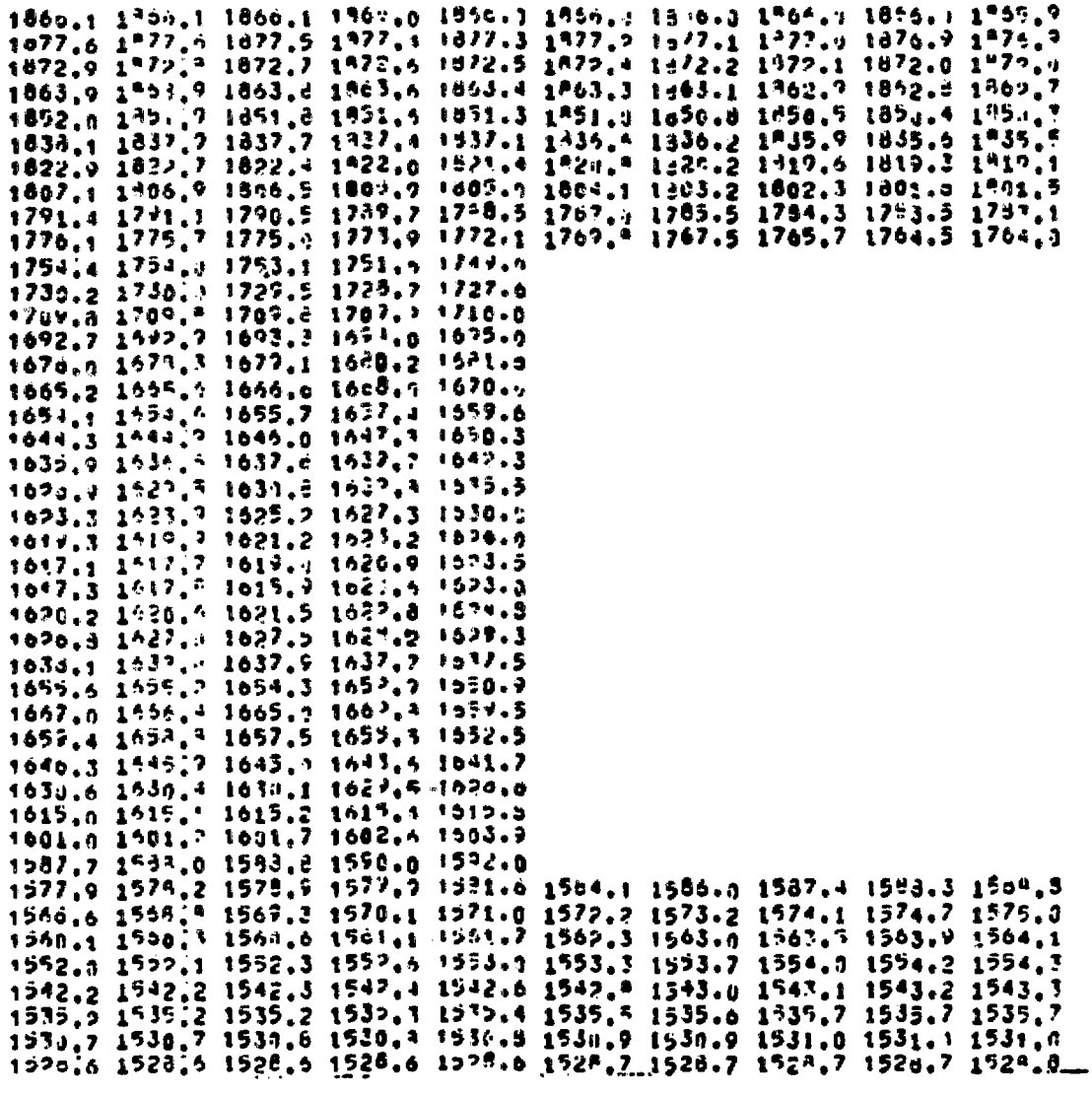

Figure 8

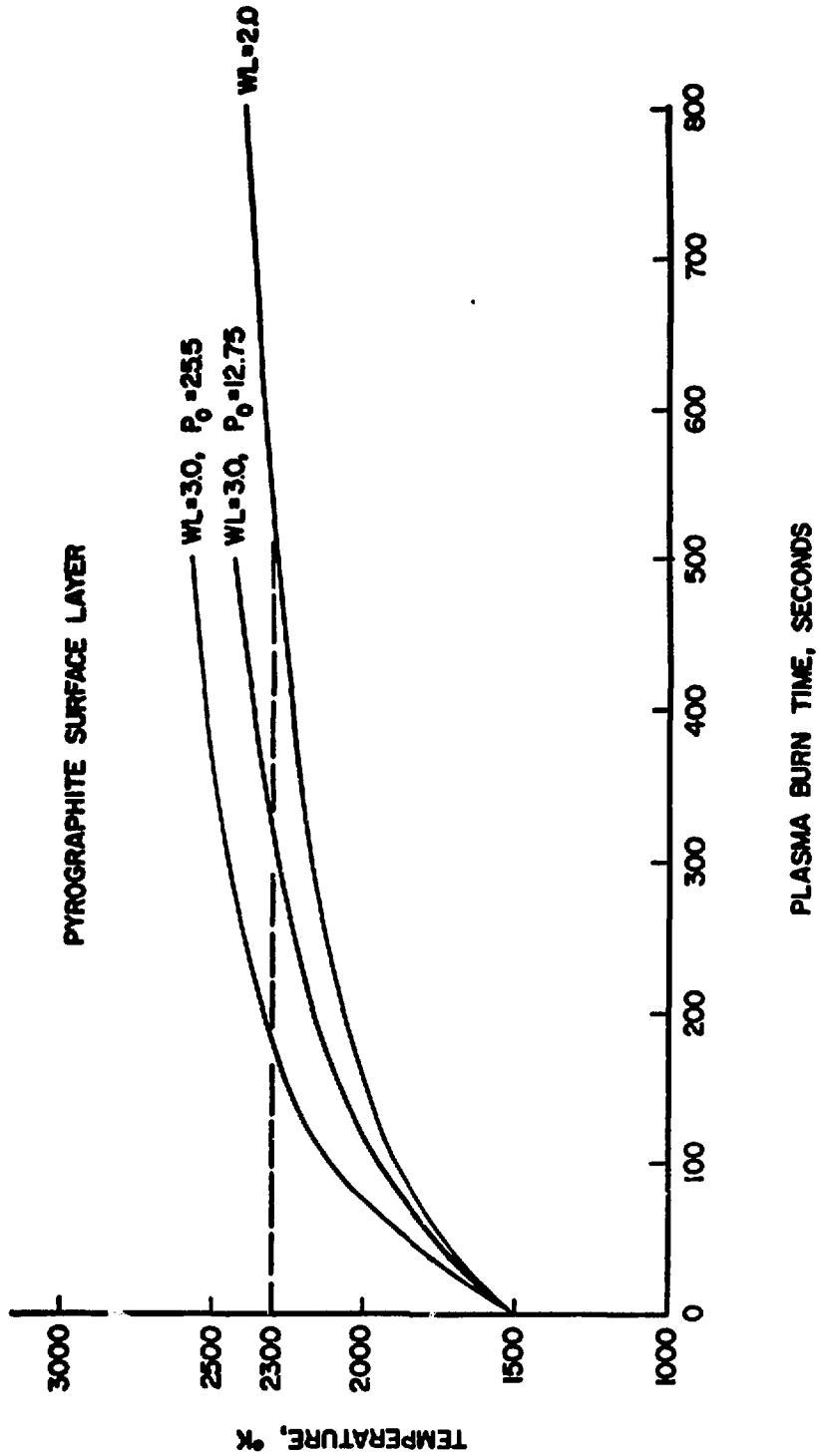

Figure 9

J. Fillo, et. al.

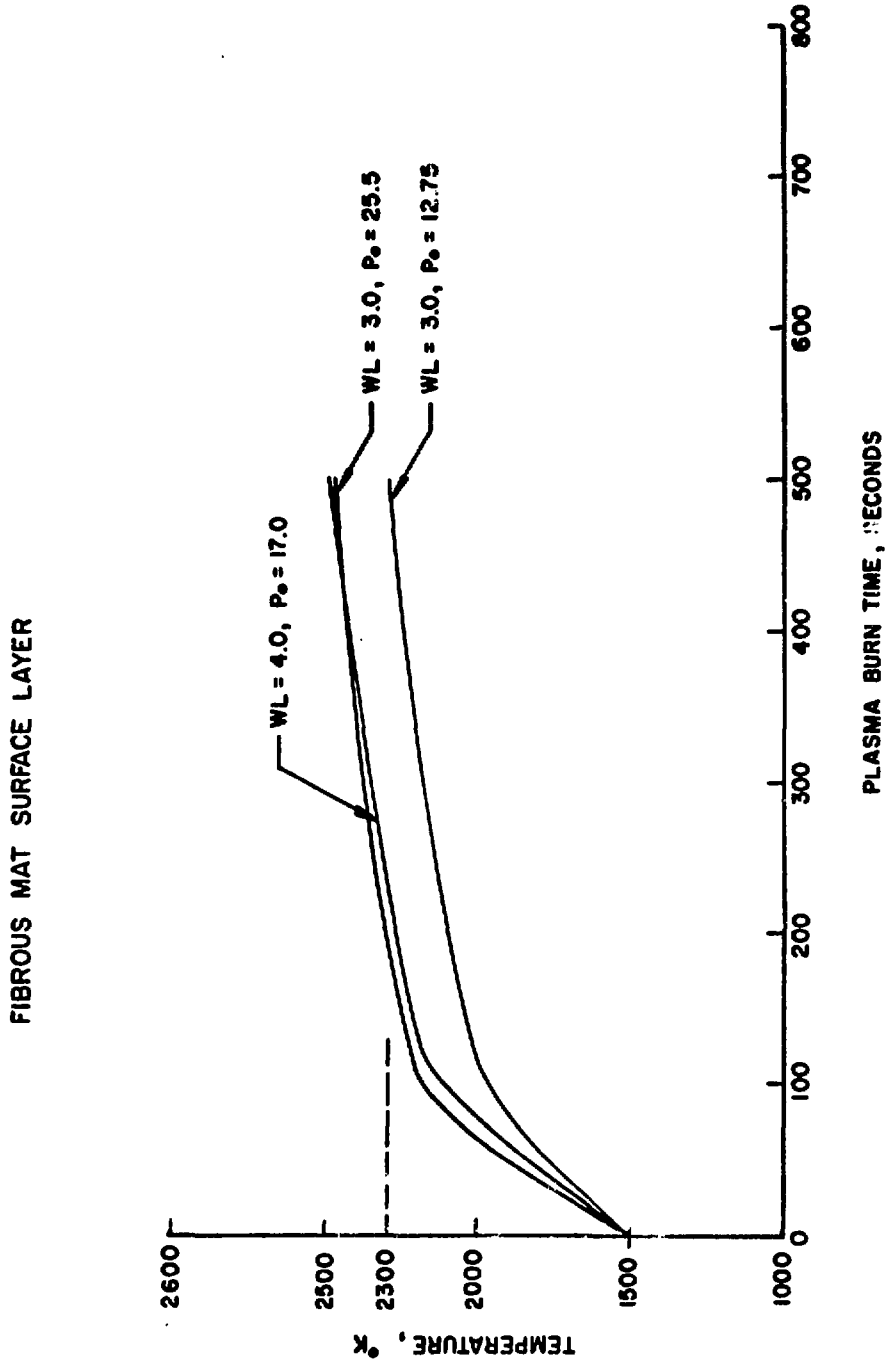

Figure 10

J. Fillo, et. al.

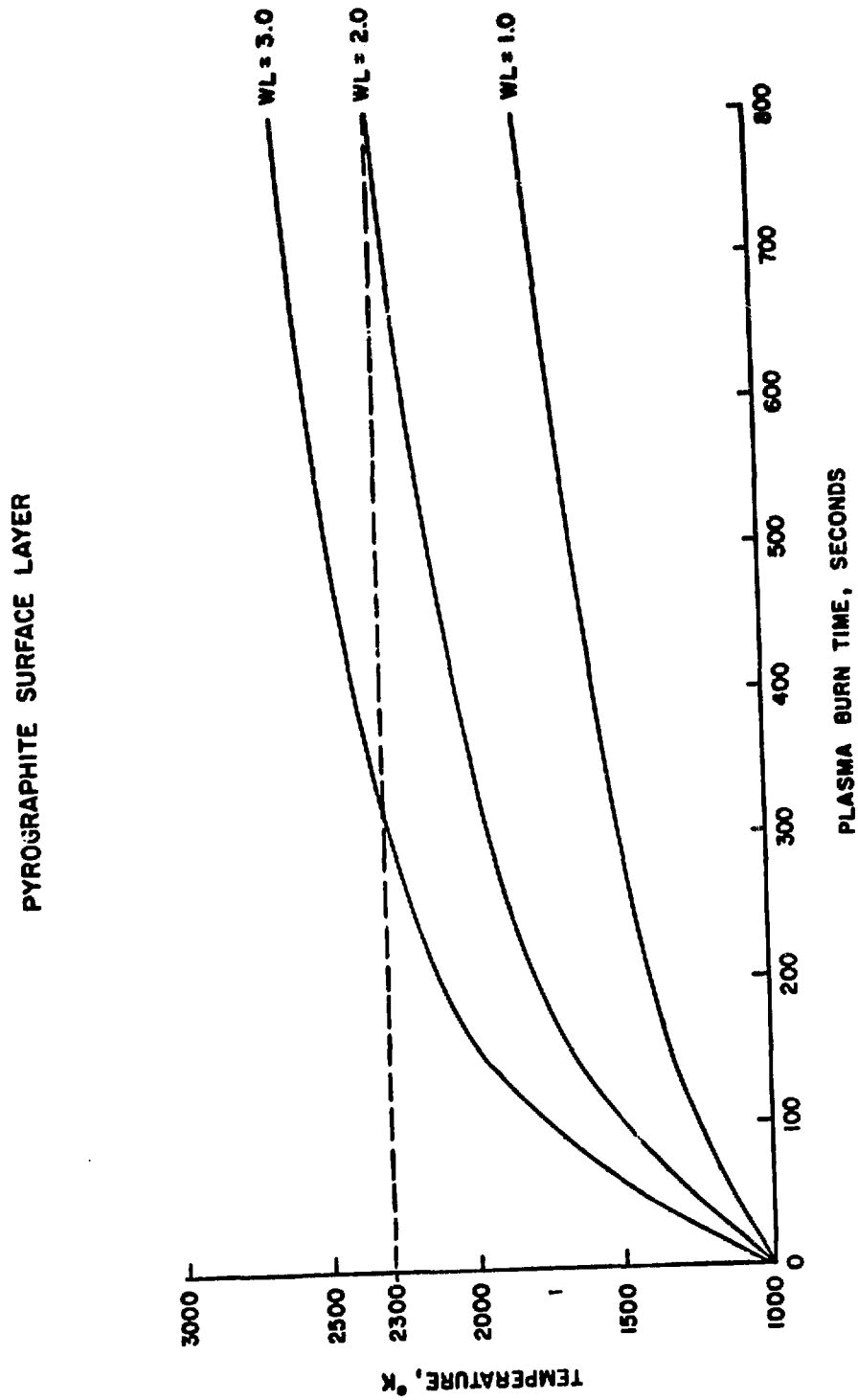

Figure 11

J. Fillo, et. al.

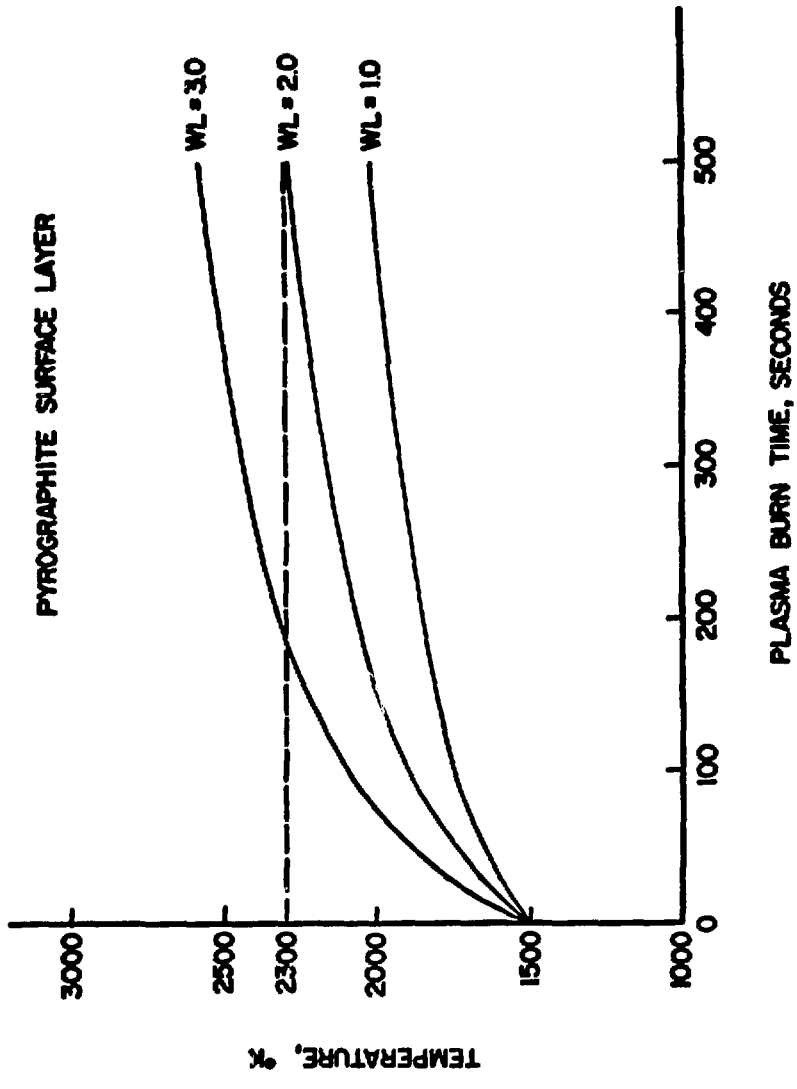

Figure 12

J. Fillo, et. al.

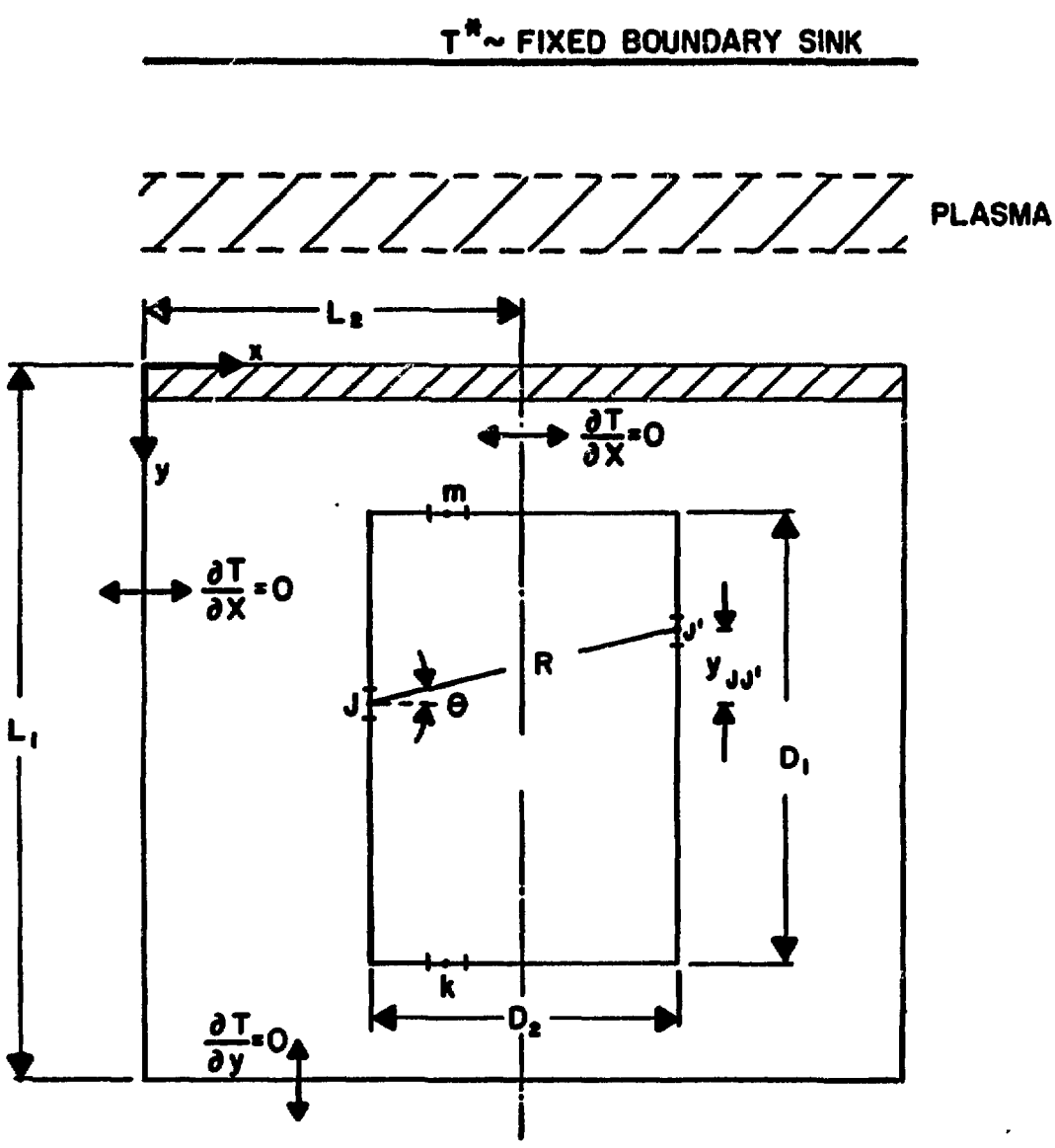

Figure 13

J. Fillo, et. al.